Highly stable low-strain flexible sensors based on gold nanoparticles/silica nanohelices

Antoine Amestoy, Aarushee Rangra, Vincent Mansard, Marie-Hélène Delville, Fabrice Severac, Emilie Pouget, Estelle Mazaleyrat, Daisuke Saya, Christian Bergaud, Reiko Oda

▶ To cite this version:

Antoine Amestoy, Aarushee Rangra, Vincent Mansard, Marie-Hélène Delville, Fabrice Severac, et al.. Highly stable low-strain flexible sensors based on gold nanoparticles/silica nanohelices. ACS Applied Materials & Interfaces, 2023, 15 (33), pp.39480-39493. ⟨10.1021/acsami.3c05852⟩. ⟨hal-04187756⟩

HAL Id: hal-04187756
https://hal.science/hal-04187756v1

Submitted on 29 Aug 2023

Highly Stable Low Strain Flexible Sensors Based on Gold Nanoparticles/Silica Nanohelices

Antoine Amestoy[a,b], Aarushee Rangra[c], Vincent Mansard[c], Daisuke Saya[c], Emilie Pouget[b], Estelle Mazaleyrat[d], Fabrice Severac[d], Christian Bergaud[,c], Reiko Oda*[,b] and Marie-Hélène Delville*[,a]*

[a] CNRS, Univ. Bordeaux, Bordeaux INP, ICMCB, UMR 5026, 87 avenue du Dr. A. Schweitzer, Pessac, F-33608, France.

[b] CNRS, Univ. Bordeaux, Bordeaux INP, Chimie et Biologie des Membranes et des Nanoobjets, 33607 Pessac, France

[c] Laboratoire d'Analyse et d'Architecture des Systèmes, LAAS-CNRS, University of Toulouse, 7 avenue du Colonel Roche, Toulouse, F-31400, France

[d] NANOMADE LAB, 3 rue des Satellites, Toulouse, F-31400, France

KEYWORDS: strain sensor, silica nanohelices, gold nanoparticles, self-assembly, dielectrophoresis, flexible electronics

ABSTRACT:

Flexible strain sensors based on nanoparticle (NP) arrays show great potential for future applications such as electronic skin, flexible touchscreens, healthcare sensors, and robotics. However, even though these sensors can exhibit high sensitivity, they are usually not very stable under mechanical cycling and often exhibit large hysteresis, making them unsuitable for practical applications. In this work, strain sensors based on silica nanohelices (NHs) arrays grafted with gold nanoparticles (AuNPs) can overcome these critical aspects. These 10 nm AuNPs are functionalized with mercaptopropionic acid (MPA) and different ratios of thiol-polyethylene glycol-carboxylic acid (HS-PEG7-COOH) to optimize the colloidal stability of the resulting NH@AuNPs nanocomposite suspensions, control their aggregation state and tune the thickness of the insulating layer. They are then grafted covalently onto the surface of the NHs by chemical coupling. These nanomaterials exhibit a well-defined arrangement of AuNPs, which follows the helicity of the silica template. They are then aligned by dielectrophoresis (DEP) between interdigitated electrodes on a flexible substrate. The flexibility, stability, and especially the sensitivity of these sensors are then characterized by electromechanical measurements and scanning electron microscopy observations. These strain sensors based on NH@AuNPs nanocomposites are much more stable than those containing only nanoparticles and exhibit significantly reduced hysteresis and high sensitivity at very slight strains. They can keep their sensitivity even after 2 million consecutive cycles with virtually unchanged responsiveness. These improved performances come from their mechanical stability and the use of nanohelices as stable mechanical templates.

INTRODUCTION

Most strain sensors respond to deformation by changing their electrical resistance or capacitance. They allow accurate and simple measurement of strain or force with wide dynamic ranges at low fabrication costs. Strain sensors are used in a wide range of electronic devices. They are expected to become more common with the development of the Internet of Things. For example, a touch-sensitive surface uses a strain sensor integrated within a deformable surface.[1-5] An electronic skin based on highly stretchable sensors is used for physical rehabilitation and motion recognition. For example, health monitoring devices can measure various health metrics such as heart rate, blood pressure, and other vitals and can be used to detect potential health issues thanks to highly sensitive and low-strain sensors. [6-8] Strain sensors also help detect and prevent structural failure in buildings, aircraft, or other large mechanical systems.[9]

Highly sensitive sensors are typically made of piezoresistive materials, whose resistance varies with strain. In the last decade, nanoobjects-based arrays have emerged as the most promising piezoresistive materials for strain sensors.[10-18] Among these nanoobjects, we find silver nanowires, reduced graphene oxide flakes, and carbon nanotubes.[3, 6, 19-20]As mentioned by Huang *et al.,* efforts have also been made to improve, for example, the sensing properties of AuNPs-based strain sensors by using different coated or interconnected organic sulfur-based ligands including 8-mercapto octanoic acid,[21] 1,9-nonadithiol,[22-23] or mercaptopropionic acid.[24]

However, the potential of the intrinsic mechanical properties of these organic linkers has never been used because of a limited gauge factor (GF ≈ 10–50). The use of tetra(ethylene glycol) dithiol (SH–TEG–SH) as a linker allowed Huang's group to reach a higher gauge factor (GF of 126, well above the background noise) with high flexibility, short response time (16.1 ms), and claimed robustness (> 2000 cycles). Such sensors based on gold nanoparticles (AuNPs) are of particular interest because AuNPs can be synthesized using simple and well-known procedures with high control over particle size and morphology, and exhibit high stability in colloidal suspensions.[25] The high sensitivity observed for the strain sensors based on nanostructured thin films[6, 10, 24, 26-30] is attributed to the tunneling of interparticle electrons and then strongly depends on the interparticle distance or tunnel barrier (d).[26] To achieve the required distance for tunneling current in nanoparticle assemblies, AuNPs must be functionalized with organic molecules or non-conductive polymers.[11, 24, 31] This surface modification improves their stability and modifies their surface with the desired function, which can easily bind to various substrates and in our case, to the amine-modified silica surface.[32-33] To form AuNPs assemblies, various methods can be used, such as layer-by-layer deposition,[23] spin coating,[16] Langmuir-Blodgett technique,[21] or convective self-assembly.[34]

Gold nanoparticle-based sensors exhibit a high gauge factor (GF) defined as $GF = \Delta R/R_0/\varepsilon$, where ΔR (%) is the relative change in the resistance and ε (%) the strain, which can range from 10 to 250 depending on the nanoparticle size, ligand, assembly density, applied strain, substrate thickness, etc (**Table 1**). However, for a strain sensor, high sensitivity *is not the only* parameter to consider for its applicability. **High stability** is also a key feature for accurate strain long-term measurements. Unfortunately, most nanoarray-based sensors exhibit low stability with rapid resistance degradation when subjected to strain loading/unloading cycles. This behavior is mainly due to irreversible displacement or localized rearrangement of clusters within the nano-assembly. In the literature, the vast majority of studies only mention tests over a few thousand cycles and very rarely on several tens of thousands of cycles[35], which does not allow a relevant definition of sensor stability for real-world applications (**Table 1**).[12]

Table 1: Comparison of low-strain flexible sensors

Material	Strain	Gauge Factor	Mechanical Testing	References
Au-coated microparticles (diameter 3.25 µm)	0-0.05% Up to 0.3%	GF = 56	2500 cycles	[36]
Boron-doped diamond nanosheets	Up to 0.55%	16 < GF < 66	5 min	[37]
Silver nanocrystals	0-0.4% With pre-strain 2%	GF = 274	1000 cycles	[31]-
Chromium NPs	Up to 0.3% Up to 3%	GF = 20 GF = 400	1000 cycles	[38]
Gold NPs	Up to 0.3%	GF = 270	25 cycles	[34]
Platinum NPs	Up to 0.1%	GF = 75	No testing	[28]
Microcracked Au Nanofilms	Up to 0.6%	GF = 76	18,000 cycles	[39]
Gold NPs	0.02 - 0.3%	GF = 250[a]	10,000 cycles	[35]
Palladium NPs	0.06 -0.2 %	GF = 390	100 cycles	[40]
Silver nanowires	0.1-360 %	>16,000	10,000 cycles	[41]
NHs@AuNPs	0.006%	GF = 120	2 000 000 cycles	This work

[a] substrate thickness: 36µm

This paper presents an original strategy to improve mechanical stability and reduce the hysteresis of sensitive strain sensors. This strategy consists in using flexible silica nanohelices as a substrate for the deposition of gold nanoparticles (AuNPs) and depositing them between electrodes by dielectrophoresis (DEP). This provides sensors with GF of 120 for NPs of 10 nm diameter (compare to ref [34]) and a cyclability of 10^6 cycles (compare to ref [35]). The grafting of AuNPs coated with insulating ligands onto the silica nanohelices (NHs) gives rise to NH@AuNPs nanostructures, where the silica NHs with a diameter of 36 nm and a length of a few micrometers are produced by the inorganic replica of the self-assembly of a chiral surfactant.[32, 42-43] A high density of 10-nm AuNPs functionalized with a mixture of ligands short enough to promote tunneling conduction is then grafted onto the surface of the silica NHs using a chemical protocol optimized from previous work.[33] The gold nanoparticle grafted nanohelices (NH@AuNPs) are then deposited in a controlled way onto interdigitated electrodes by dielectrophoresis (DEP). Finally, electromechanical characterization of strain sensors fabricated with NH@AuNPs is performed.

In this work, the great benefit of such an approach is demonstrated in the fabrication of strain sensors with not only high-gauge-factor (>100), but also improved mechanical stability, and reduced hysteresis. NHs grafted with AuNPs (NH@AuNPs) combine three major advantages: (1) ligands-coated AuNPs generate high piezoresistivity through tunneling conduction with controlled inter-AuNP distance and ensure high sensitivity; (2) NHs provide mechanical cohesion with stable AuNP arrangement and ensure the stability of AuNPs nanoarrays; (3) NH@AuNPs remain however highly deformable thanks to their helical shape and their high aspect ratio.

RESULTS AND DISCUSSION

Synthesis and functionalization of AuNPs with different ratios of SH-PEG$_7$-COOH and MPA.

AuNPs with a diameter of 10 nm were synthesized according to the procedure reported by Slot and Geuze[44] consisting of the reduction of potassium tetrachloroaurate ($KAuCl_4$) using tannic acid (TA) as a reducing agent and trisodium citrate (TSC) as a stabilizing agent. The details of the synthesis are reported in the experimental section. These particles exhibit labile surface ligands that can be exchanged with more suitable ligands: O-(2-Carboxyethyl)-O’-(2-mercaptoethyl) heptaethylene glycol (SH-PEG7-COOH) and mercaptopropionic acid (MPA) by simple exposure at 400 rpm overnight at 4°C.[32] Both ligands end with a thiol group and a carboxyl group, (**Figure 1a**) the thiol one being much more efficient as a ligand due to the well-known affinity of gold surface for sulfur. This does not change the carboxylate functionalization of the gold NPs but allows a covalent bonding *via* the sulfur functional group as compared to the weak link provided by the citrate anion. The 10 nm diameter of the AuNPs was chosen for two main reasons: (i) previous studies showed that increasing the size of AuNPs led to an increase in the value of the Gauge Factor (GF),[34] (ii) meanwhile, AuNPs with diameters larger than 10 nm induced inhomogeneous adsorption around nanohelices (diameter ~ 36 nm), resulting in a lower density of AuNPs on the silica surface.[43]

To tune the interparticle distance after grafting, the AuNPs were functionalized with different ratios of HS-PEG$_7$-COOH and MPA as illustrated in **Figures S1, and S2** which respectively show the UV-vis spectra of the gold nanoparticles modified with respectively molar %: 100% MPA, 50%MPA50%PEG, and 100%PEG (**Figure S1**) and their TEM images. These images illustrate the respective ability of these ligand ratios to separate the AuNPs on the TEM Grid (**Figure S2**). Moreira *et al.* showed that arrays of AuNPs protected by thiol ligands yielded high-sensitivity gauges that depended on the ligand length.[24] To find the optimal ligand composition, AuNPs were functionalized with different molar ratios of MPA (short) and HS-PEG$_7$-COOH (PEG) (long) ligands. Samples are named MPA$_{100}$, MPA$_{75}$PEG$_{25}$, MPA$_{50}$PEG$_{50}$, and PEG$_{100}$ for respectively the 0%, 25%, 50%, and 100% of the PEG ligand **(Figure 1a)**.

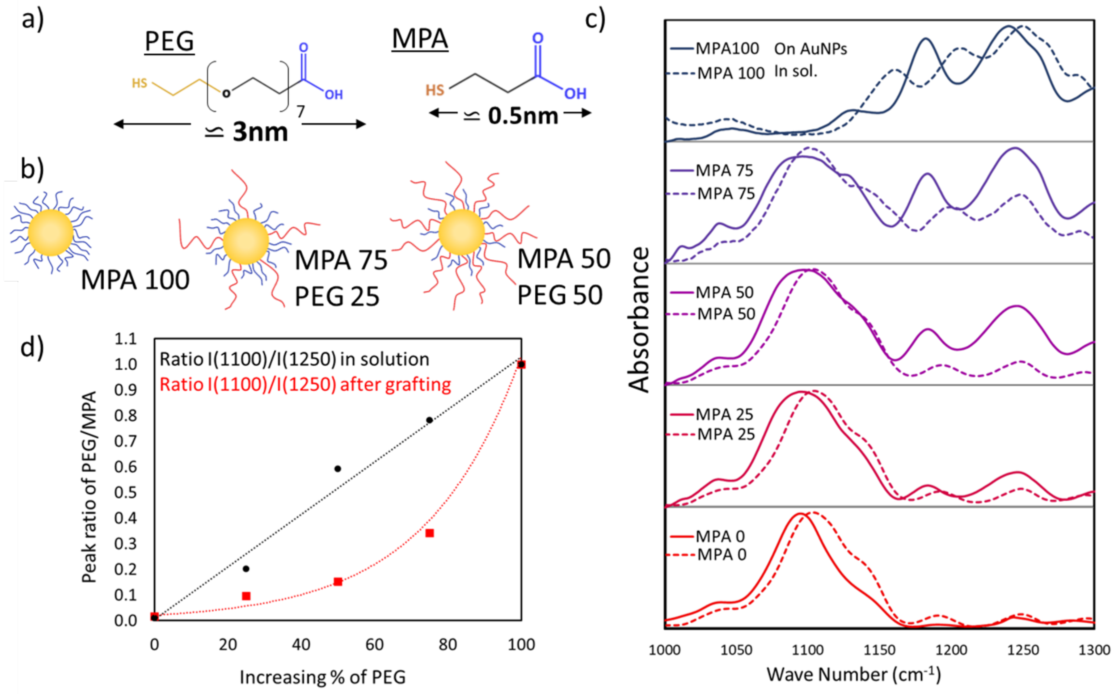

Figure 1. a) Chemical representation of mercaptopropionic acid and thiol-polyethylene glycol-carboxylic acid and their approximate length. b) Schematic representation of AuNPs functionalized with different ratios of MPA and HS-PEG_7-COOH. c) FTIR spectra of different MPA and HS-PEG_7-COOH ratios in solution (dashed lines) and the corresponding suspensions once grafted on the AuNPs (full lines). d) Peak ratio of the 1100 cm^{-1} *vs.* 1250 cm^{-1} bands as a function of the fraction of HS-PEG_7-COOH (PEG) for the ligand solution before functionalization (black) and the functionalized AuNPs after being rinsed (red).

Competitive molecular adsorption studies on AuNPs were performed by Attenuated Total Reflectance-Fourier Transform Infrared (ATR-FTIR) spectroscopy (**Figure 1b,c**). For pure MPA solution, the significant absorbance near 1,250 cm^{-1} corresponds to the C-O stretching of the carboxylic group in MPA. For pure HS-PEG_7-COOH, the absorbance observed near 1,100 cm^{-1} is characteristic of the C-O stretching in the PEG chain. The comparison of the spectra of the AuNPs-free solutions (before grafting) and the suspensions (after grafting and rinsing) (**Figure 1c**) shows a change in the signal intensity with an increase in the intensity of the peak at 1,250 cm^{-1} after functionalization. This indicates that the fraction of PEG ligands grafted onto the AuNPs is lower than that in the solution. To obtain quantitative information, the normalized ratios between the two peak intensities were estimated (**Figure 1d**) both in solution and on the particle surface. A good agreement between the peak ratio and the fraction of HS-PEG7-COOH added is observed in the solution. This demonstrates the ATR-FTIR measurement is well suited to measure the ligand ratio. The peak ratios of the grafted suspensions show that this variation is no longer linear, and $MPA_{75}PEG_{25}$ and $MPA_{50}PEG_{50}$ have grafted PEG ligand ratios of only 10% and 15% respectively.

The smaller size of MPA compared to HS-PEG_7-COOH makes it more mobile in solution, so it can reach the AuNPs surface and react much faster. In addition, several studies have shown a relationship between the size of the ligands and their maximum grafting density.[45-47] The longer the ligand, the lower its grafting density. In the case of MPA and SH-PEG_7-COOH, the difference in size is significant, so when the SH-PEG_7-COOH ligand has reached its maximum grafting density, the MPA ligand can continue to graft to the AuNPs surface and achieve a higher grafting density.

Synthesis and chemical modification of the silica NHs. The formation of silica nanohelices (NHs) has already been published several times.[42, 48] To summarize, a positively charged 16-2-16 Gemini surfactant of formula C_2H_4-1,2($(CH_3)_2N^+C_{16}H_{33})_2$, is complexed with a chiral tartrate counter-ion to generate in water supramolecular assemblies in the form of twisted or helical nanoribbons depending on the experimental conditions (with the generic name of **nanohelices**) (**Figure S3a**). Depending on the chirality of the *L*- or the *D*-tartrate, the handedness of the helix is accessible and perfectly controlled (right- and left-handed for *L*- and *D*-tartrate respectively). The silica transcription of such supramolecular assemblies gives rise to the formation of silica nanohelices with the same handedness and morphological control.).

The silica transcription of such supramolecular assemblies gives rise to the formation of silica nanohelices with the same handedness and morphological control.[33, 48]

Grafting of AuNPs on the surface of NHs. The silica structures were then modified with (3-aminopropyl) triethoxysilane (APTES) to enrich the surface with amine groups and proceed to a covalent chemical coupling with gold nanoparticles.[33] The formation of a covalent peptide bond between the acid function of the AuNPs and the amino groups on the nanohelix requires the initial activation of the acidic groups based on well-established processes[49-51] using 1-ethyl-3-(3-dimethyl aminopropyl)-carbodiimide hydrochloride (EDC.HCl) and *N*-hydroxy succinimide (NHS) as typical agents to activate the -COOH group. Even though it is a process largely described in the literature, it was adapted to the nature of the ligand at the surface of the NP. First, a 3h pre-aging of the EDC/NHS mixture at 4°C showed a positive action on the aggregation state of the AuNPs and this, regardless of the ratios of EDC/NHS used in the different reactions. Optimal conditions are summarized in **Table 2** and illustrated in **Figure 2** and **Figure S3** as explained below, each condition being repeated at least 3 times.

Table 2. Optimal grafting conditions of AuNPs on the surface of NHs, depending on their surface composition.

AuNPs@	C(AuNPs)	Activation	C(activation)	C(NHs)
MPA_{100}	140 nM	EDC/NHS	1.2/6.0 mM	100 µg/mL
$MPA_{90}PEG_{10}$	140 nM	EDC/NHS	1.2/6.0 mM	100 µg/mL
$MPA_{75}PEG_{25}$	140 nM	EDC/NHS	12/60 mM	100 µg/mL
$MPA_{50}PEG_{50}$	140 nM	EDC/NHS	12/60 mM	100 µg/mL
PEG_{100}	140 nM	EDC/NHS	12/60 mM	100 µg/mL

140 nM

Figure 2a describes the overall synthesis and surface modification with different ligand ratios, the nanoparticles are covalently attached to amino-modified nanohelices by activation of the carboxylate with EDC/NHS.[33, 49-50] **Figure 2b-e** illustrate the grafted NHs produced with various ligand ratios:NH@MPA_{100}, NH@$MPA_{75}PEG_{25}$, NH@$MPA_{50}PEG_{50}$, andNH@PEG_{100}.

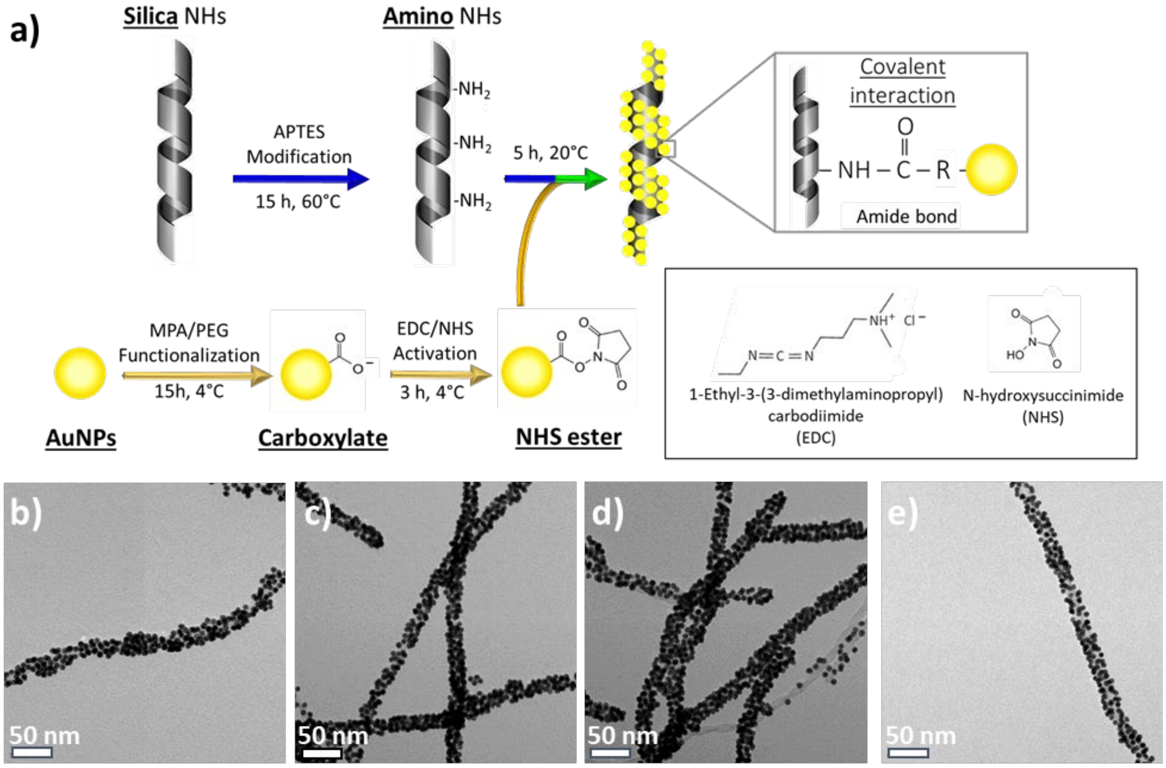

Figure 2. a) Principle of modification of silica helices with gold nanoparticles. TEM images of NH@AuNPs with different compositions of ligand at the surface of AuNPs. The MPA to SH-PEG$_7$-CO$_2$H molar ratio varies from b) 100:0, c) 75:25, d) 50:50, and e) 0:100 using optimized conditions from **Table 2**.

NH@MPA$_{100}$ exhibits either a homogeneous density of grafted particles at the surface of NHs (**Figure 2b (**EDC/NHS 1.2/6.0 mM) or a strong aggregation of the AuNPs resulting in the formation of an inhomogeneous coating around the NHs and aggregation of the nanocomposite when the EDC/NHS concentration is 10 times higher (**Figure S3e**). The addition of different amounts of PEG at the surface of the AuNPs during functionalization allows a more homogeneous density of grafted particles (**Figure 2c,d**) for a 12/60 mM EDC/NHS ratio, with the formation of a monolayer of AuNPs around the NHs, while a 10 times smaller one leads to insufficient grafting ((**Figures S3b,c**). When HS-PEG$_7$-COOH is used on its own, NH@PEG$_{100}$ exhibits a low density of AuNPs with free space still available on the silica surface (**Figure 2e**); this large interparticle distance will be detrimental for further conduction processes as illustrated later on (*vide infra*).

The covalent grafting of the AuNPs at the surface of the silica NHs has been attested by ATR Infra-Red spectroscopy, by comparison with our previous work.[33] In **Figure 3,** the peaks at 1,640 cm^{-1} and 1,540 cm^{-1} are attributed to the associated forms of –CONH amide band I group and the N–H amide band II group, respectively confirming the covalent nature of the bond between the nanohelix and the gold nanoparticle; the peak at 1,255 cm^{-1} is attributed to the –C–N stretching of the same amide bond. Peaks at 1,078 cm^{-1}, 2,853 cm^{-1}and 2,907 cm^{-1} are characteristics of the Si-O vibrations and the C-H stretching of CH_2 groups respectively **(Figure S4a**). On the contrary, the peak of the ν_{COOH} stretching vibration at 1,716 cm^{-1} is much smaller, indicating that the major part of the carboxylic groups of the MPA ligands has reacted with the NHS to form the amide bonds. **Figure S4b** parallelly shows the variation of the ATR spectra of MTA with grafting on gold nanoparticles and further reaction on silica helices. Similar results are obtained for a mixture of MPA and PEG (results not shown).

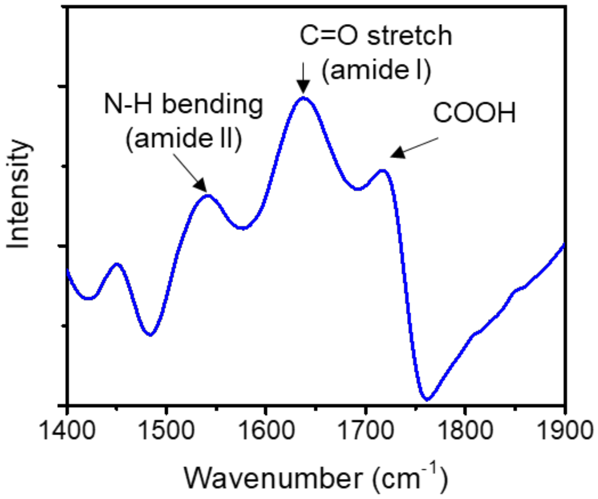

Figure 3. An example of the ATR infrared spectrum sample from **Figure 2b** shows the covalent grafting of AuNPs@MPA_{100} on NHs.

The chiroptical properties of NHs@AuNPs were then studied since the data obtained by UV-vis absorbance and circular dichroism (CD) allow us to obtain information on the interaction between the nanoparticles. Metal NPs exhibit a very strong surface plasmon resonance, widely used in surface exalted Raman spectroscopy (SERS).[43] The plasmon coupling between two gold nanoparticles is very sensitive to the distance between them and when two plasmonic particles get closer, their resonances couple leading to an increase in the signal and a redshift of the resonance wavelength.[52] This property has allowed the development of colorimetric biosensors and molecular rulers.[53]

As mentioned above, the AuNPs with different ratios of MPA and PEG, have a UV-vis absorbance spectrum with a maximum absorbance wavelength centered at 520 nm (**Figure S1**). On the other hand, an immediate color change is observed as soon as they are grafted onto the surface of the nano-helices (**Figure S5)** confirming the redshift in the UV-vis absorbance spectra of NH@AuNPs for the different surface compositions of AuNPs. This redshift of the band effectively shows a link between the increase in the amount of MPA on the AuNPs and a decrease in the interparticle distance on the surface of the helices. A broadening of the plasmonic band with the increase in MPA and the concomitant decrease in SH-PEG-COOH is also observed. Such a decrease in SH-PEG-COOH decreases the steric repulsions of the AuNPs, which can get closer to each other on the surface of the nanohelices. Moreover, the broadening of the plasmon band can be explained by (i) the high number of AuNPs on the surface of the nanohelices and (ii) the grafting inhomogeneity with the formation of AuNP clusters separated by various distances.

Deposition of the nanohelices (NH@AuNPs) by dielectrophoresis.[54-57] The last step of the fabrication of the strain sensors consists of the deposition of the nanocomposites between interdigitated electrodes. Metallic interdigitated electrodes were fabricated on a 125 μm-thick flexible polyimide (PI) film using the standard microfabrication technique (**Figure S6a-b**). The active area of the sensor is 16 mm^2. Different designs of interdigitated electrodes have been tested with different gaps and the configuration with 3-µm-gap and square-shaped electrodes gave the best results (**Figure 4a-c**, and **Figure S6c**).

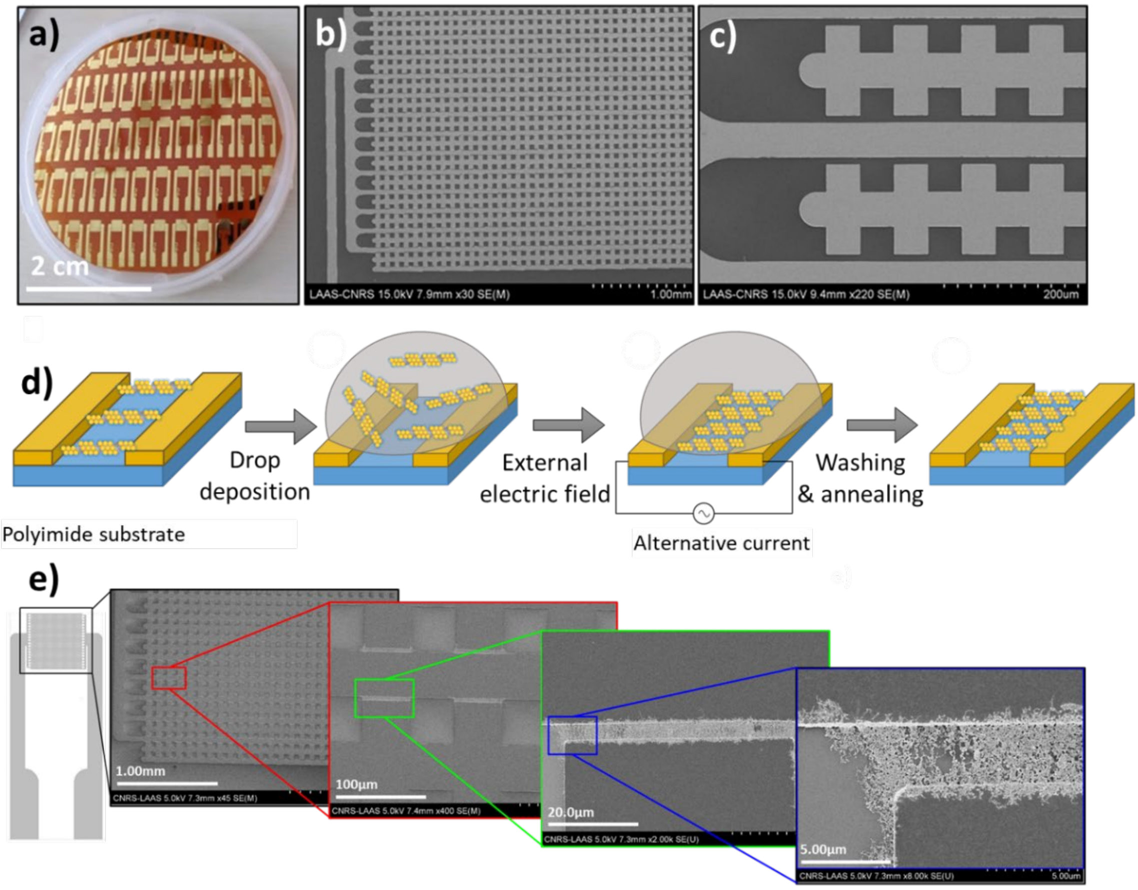

Figure 4. (a-c) Images of the metallic interdigitated electrodes before deposition: a) optical image of electrodes on a 4 inches (10.16 cm) PI substrate; b) SEM picture of the active area; c) close-up view of a close-up view of 3µm-spaced interdigitated electrodes. d) Schematic representation of the deposition of nanohelices grafted with modified gold NPs (NH@MPA$_{50}$PEG$_{50}$) using DEP. e) SEM images of the electrodes and gaps between electrodes after deposition at different magnifications. A 20-µL drop of NH@MPA$_{50}$PEG$_{50}$ at 0.01 mg/mL in water was deposited on the electrodes, an alternating current was then applied across the electrodes, for 30 seconds, with an amplitude of 500 mV, and a frequency of 35 kHz. After turning off the current, the electrodes were rinsed with ethanol and dried.

Deposition of the NH@AuNPs is performed by dielectrophoresis. This technique enables the increase of the nanoobjects concentration in the area between electrodes with controlled orientation, particularly in the case of anisotropic objects. Indeed, the AC voltage induces a dipole moment in the nano-objects in the suspension. The induced dipole interacts with the applied electric field leading to a translational motion towards the high electric field region - between the electrodes- and a parallel alignment to the electric field. SEM images (**Figure 4e**) show that the NH@AuNPs are strongly localized in the small gap separating the electrodes. In comparison, a deposition by drop-casting (without any applied field) results in particles randomly distributed everywhere on the substrate (**Figure S7**). This highly localized deposition is a strong advantage of the DEP technique, which optimizes the small quantity of material. A 20-µL drop of nanohelices suspension in water is used to cover the interdigitated electrode (**Figure 4d**). An AC voltage is applied between the electrodes for a given time (from 10 s to 1 min). The drop is then removed, and the sensor is allowed to dry at room temperature under nitrogen flow. The quality of the DEP assembly depends mainly on four parameters: the applied external voltage, the frequency, the suspension concentration, and the deposition time. The optimum assembly is obtained for an applied voltage of 10 $V_{p\text{-}p}$ and a frequency of 35 kHz. A concentration of 0.01 mg/mL results in a homogeneous assembly. Higher concentrations led to a swift deposition resulting in poor control of the deposition. With lower concentrations, the deposition is slow and can take several minutes.

The NHs deposited with this method, form assemblies of relatively well-aligned bridges between the two electrodes, and each bridge is formed with several entangled nanohelices. **Figure 5a-c** show the gradual deposition on the electrodes, with deposition times of 10 s, 30 s, and 50 s. First, a few connections quickly form. New bridges then go on to grow independently of the initial ones. Eventually, the density of bridges is high enough to cover the entire inter-electrode gap homogeneously.

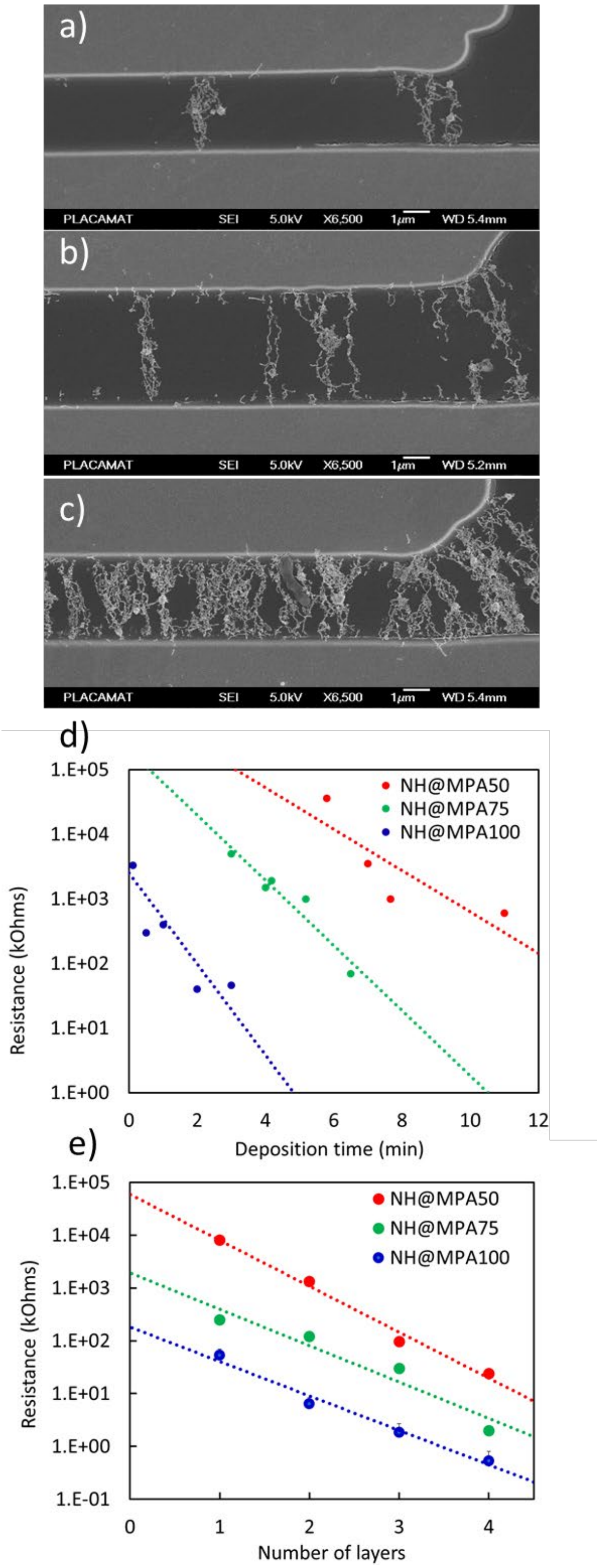

Figure 5. (a-c) SEM pictures of the deposition of NH@ MPA100 by DEP on interdigitated electrodes after a) one deposit, b) three deposits, and c) five 10-second deposits. Scale bars 1 μm. (d-e) Variation of the resistance with d) the deposition time t_d and, e) the number of layers

N_{layer} for (blue) MPA_{100}, (green) $MPA_{75}PEG_{25}$, and (red) $MPA_{50}PEG_{50}$. The dotted lines are exponential fits.

These results highlight the efficiency of the DEP technique because all the objects are deposited directly in between and only in between the electrodes, *i.e.*, on the sensor's active area. Therefore, all the nano-objects actively participate in the deformation detection.

The variation of the initial resistance R_0 (after removing the suspension drop and drying the sensor) exhibits a swift exponential decrease with time, for all the various ligand compositions (**Figure 5d**), a decrease consistent with the gradual formation of bridges observed during the deposition. The deposition rate is highly impacted by the nature of the ligand around the gold NPs. With a higher proportion of the long ligand (PEG), the decrease in resistance gets slower (**Figure 5d,e** red dots**)** as shown by the comparison of the rates of decrease in resistance between NH@MPA_{100}, NH@$MPA_{75}PEG_{25}$, and NH@$MPA_{50}PEG_{50}$. To reach a resistance of 500 kΩ, only 1 min is needed for NH@MPA_{100}, while 5 and 11 min are respectively required for NH@$MPA_{75}PEG_{25}$ and NH@$MPA_{50}PEG_{50}$. However, with NH@MPA_{100}, the grafting allows short inter-particle distance, resulting in a globally high conductivity (**Figure 2b,** and blue curve in **Figure 5d,e**). The use of increasing amounts of PEG ligand on the surface of the gold NPs (NHs@$MPA_{75}PEG_{25}$ and NH@$MPA_{50}PEG_{50}$) (**Figure 2c,d,** and green and red curves in **Figure 5d,e**) prevents long-term potential aggregation due to short ligands but also increases the inter-particle distance resulting in lower conductivity. For the NH@PEG_{100}, a resistance of $4\ 10^4$ Ohms was obtained and no decrease at all in the resistance could be reached even after an hour of deposition or up to 10 10s-deposits; the interparticle distance between the AuNPs was too large (**Figure 2e**) to allow any tunneling effect and then the fabrication of a sensor.

A protocol was thus developed to tune precisely the initial resistance, performing deposition through successive layers based on three PEG ratios (0, 25, and 50%) (**Figure 5e**). Each layer corresponded to a DEP deposition during a well-controlled time. Between each layer, the subsequent steps are performed: remove the excess liquid, dry the sensor at room temperature, measure the initial resistance, and then add another drop of fresh suspension for deposition of the subsequent layer. The deposition time is short enough to obtain a small variation of the resistance between each step (10 s, 30 s, and 60 s for respectively NH@MPA$_{100}$, NH@MPA$_{75}$PEG$_{25}$, and NH@MPA$_{50}$PEG$_{50}$). An exponential decrease of the initial resistance with the number of layers N$_{\text{layer}}$: $R_0 \propto e^{-\frac{N_{layer}}{N_0}}$ is obtained with much more precise control of the final resistance (compare **Figure 5d** and **Figure 5e**). Indeed, the measurement of the resistance after each step could allow us to adapt the subsequent step to obtain the targeted resistance.

Electromechanical characterization of the sensors.

To evaluate the sample piezoresistivity, the sensor was glued on the center of a flexible PET plate which underwent a three-point bending test. The initial resistance R$_0$ (baseline resistance recorded when the strain sensor is under no stress nor deformation) and its variation ΔR were monitored during the bending of the flexible PET substrate. The relation between the force applied to the PET plate and the strain applied to the sensor was calibrated using a commercial metallic strain sensor. The strain ranges from $\varepsilon = -1.3$ % (compressive) to $\varepsilon = +1.3$ % (tensile).

The resistance increases when the sensor is stretched and decreases when the sensor is compressed, (**Figure 6**). For all sensors, the resistance under compression and elongation is given by a simple exponential law (eq 1):

$$\frac{\Delta R}{R_0} = e^{GF.\epsilon} - 1 \qquad \text{eq 1}$$

where GF is the gauge factor, (**Figure 6b**). This exponential behavior is consistent with the electrical conduction through the tunneling effect[26, 58] where the interparticle resistance varies exponentially with the AuNPs separation. When a tensile strain is applied, the distance between adjacent NPs on the NHs increases, increasing also the resistance. When a compressive strain is applied, the NPs are getting closer, resulting in a decrease in resistance. For small strains, eq 1 simplifies to GF = $\Delta R/R_0/\epsilon$.

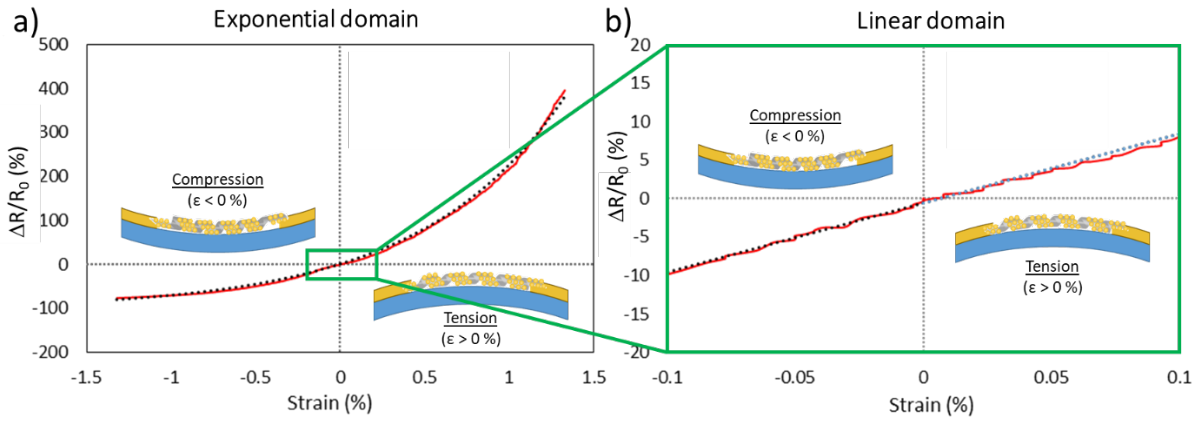

Figure 6. Relative resistance variation $\Delta R/R_0$ with the applied strain for a nanohelix-based sensor (NH@MPA$_{50}$PEG$_{50}$) with 3 layers applied on an 800 µm thick PET substrate; a) high deformation, b) low deformation. Black dots are experimental data, and the fits appear in red.

The gauge factor, GF, is extracted by fitting the measured variation of resistance using eq 1. **Figure 6** corresponds to a strain sensor with a gauge factor GF = 120, which places the sensitivity of such strain sensors among the best of those previously reported for strain gauges based on nanoparticles.[28, 34, 59-60] In comparison, the relative resistance variation of a conventional metallic strain sensor is about 100 times lower.

After showing how to control the initial resistance, R_0, using successive DEP depositions, the influence of R_0 on the sensitivity of these strain sensors was then studied. **Figure 7a** shows the variation of the gauge factor with the initial resistance for strain sensors based on three different NHs (NH@MPA$_{100}$PEG$_0$, NH@MPA$_{75}$PEG$_{25}$, and NH@MPA$_{50}$PEG$_{50}$). They all display a similar behavior: the gauge factor versus initial resistance is a bell-shaped curve, with a maximum gauge factor value reached for initial resistances ranging from 120 kΩ

($NH@MPA_{100}PEG_0$) to 800 kΩ ($NH@MPA_{50}PEG_{50}$). Subsequent depositions resulting in initial resistances below 120 kΩ caused a decrease in the gauge factor, with values sometimes as low as that of metal foils (GF = 2).

High initial resistance values correspond to low quantities of the deposited material. During the first layer of deposition, very few percolation bridges form between the electrodes, with a subsequent low electron flowing rate and a small signal-to-noise ratio. Moreover, sensors obtained in a single-deposition step have very low stability since the breakdown of any of the conduction bridges has a detrimental influence on the resistance. Sensors made with two or three deposition steps have higher quantities of deposited material and a larger number of conduction bridges. It results in a better signal-to-noise ratio and, therefore, a higher sensitivity. Further increase in the number of the deposition layers leads to a decrease in both the resistance and the gauge factor to a value close to that of metal foil strain gauges. As the quantity of deposited material increases, the aggregation of NH@AuNPs occurs, changing the effective inter-particle distance. The conduction no longer takes place through 1D bridges, but through a 2D film (and eventually a 3D layer). The confinement of electron transport weakens, leading to a decrease in sensitivity since percolation paths are less affected by strain.[24, 28, 61]

This behavior is reproducible, and **Figure 7b** illustrates the data obtained for at least ten samples of $NH@MPA_{100}PEG_0$, $NH@MPA_{75}PEG_{25}$, and $NH@MPA_{50}PEG_{50}$ sensors. The change in the ligand ratio does not influence the final properties of the optimized sensors. The maximum sensitivity of about GF = 100, is obtained for an optimal initial resistance $R_{0,\, max}$ = 100 kΩ.

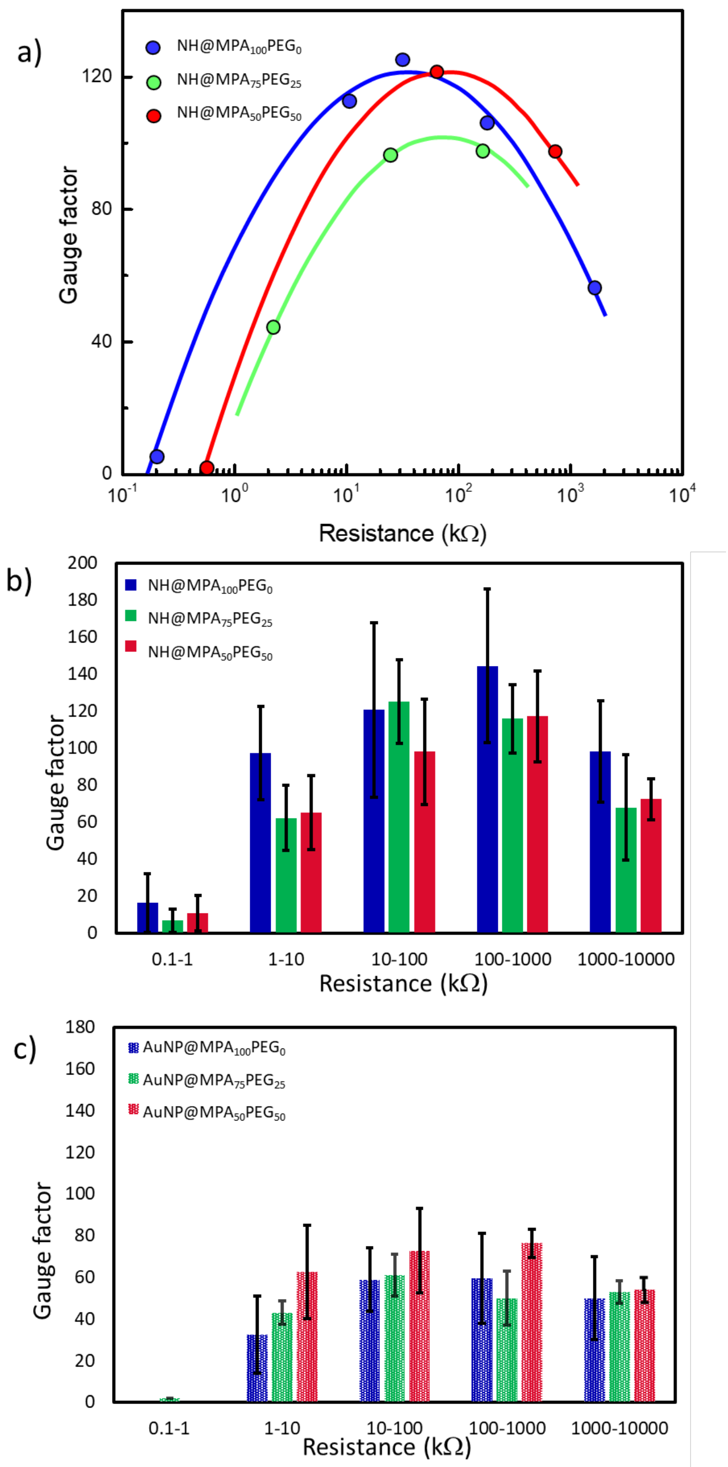

Figure 7. a) Gauge factor variation of three strain sensors based on NHs with different ligands at the surface of the AuNPs: NH@MPA$_{100}$PEG$_0$, NH@MPA$_{75}$PEG$_{25}$, and NH@MPA$_{50}$PEG$_{50}$; *curves are guides for the eyes.* b) and c) Histograms of the responses of various devices with identical composition at the gold surface with the initial resistance of the strain gauge, for b) NHs/AuNP strain sensors and c) AuNP strain sensors.

Moreover, the functionalization of AuNPs by the $MPA_{50}PEG_{50}$ ratio provides a much more reproducible as well as the best grafting on the surface of nano-helices, an improvement of great importance for the whole fabrication process.

For comparison, sensors based on AuNPs alone were also produced, using a deposition by drop-casting (**Figure 7c**). Similar trends were observed in terms of gauge factors but with much smaller standard deviations. The maximum values of gauge factors for free-AuNP sensors are around $GF_{max} = 60$, twice lower than for the NH@AuNPs sensors. The use of NHs strongly helps improve the sensitivity thanks to the differences in geometry of the conducting network. Conduction uses 1D bridges in the case of NH@AuNPs sensors, whereas for the AuNPs-based films, it uses the 2D nano-assembly. The confinement of the electron transport in a 1D path again increases the sensitivity.

To evaluate the physical robustness and reliability of these strain sensors, a series of bending cycles were performed in the tensile mode and under conditions close to their future applications. An example is given in **Figure 8** for NH@MPA_{100} and MPA_{100}-AuNPs strain sensors with similar initial resistance. They were repeatedly bent and released between $\varepsilon = 0$ % and $\varepsilon = 0.06$ % over 350 s. Sensors based on NHs (**Figure 8a,b**) exhibit a very stable and reproducible signal throughout the cycling. The resistance at rest is constant, and the relative resistance variation $\Delta R/R_0$ is highly reproducible. By comparison, when using free-AuNPs sensors (**Figure 8c**), a fast decrease of the resistance at rest and a lack of stability in the relative resistance variation is observed which makes any calibration very difficult.

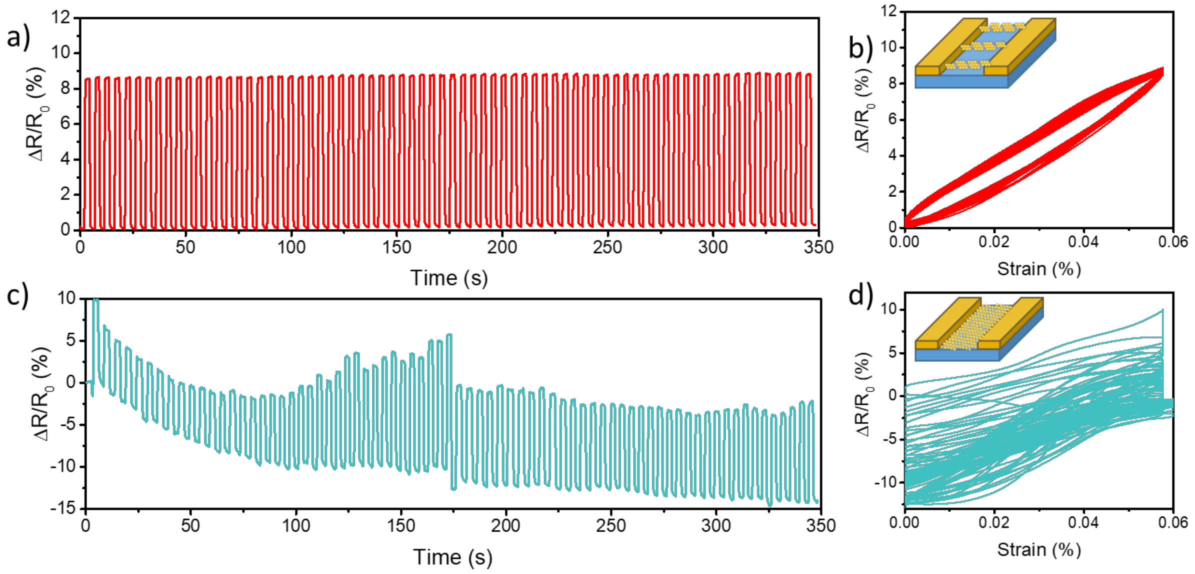

Figure 8. Time-dependent relative resistance variation of strain sensors undergoing a series of deformation cycles between $\varepsilon = 0$ % and $\varepsilon = 0.06$% for (a) an NH@MPA$_{100}$ strain sensor, (c) an AuNP@MPA$_{100}$PEG$_0$ strain sensor, and (b), (d) their corresponding relative resistance variation showing hysteresis behaviors.

The relative variation of resistance with strain associated with the loading and unloading phases (**Figure 8b,d**) highlights the respective sensors' hysteresis. A system with hysteresis has a response that depends not only on strain but also on strain history. Typical causes for hysteresis are friction and structural changes in the material. A smaller hysteresis is observed for NH@AuNPs sensors compared to free-AuNP sensors. This difference is attributed to the mechanical properties of the NHs, which provide a spring-like effect under strain and improve sensor stability. For free-AuNPs sensors, cracks and defects in the organization of the particles easily appear under strain, inducing a change in the conduction path. Therefore, both the resistance and the gauge factor change during the deformation cycle.

NHs highly increase the mechanical cohesion of the nano-assembly and prevent the formation of cracks perpendicular to the conduction paths. NHs-based sensors show a lower hysteresis, higher stability, and a more reproducible resistance variation. Eventually, preliminary tests showed that encapsulated NHs-based sensors were stable over a wide range of temperatures (from - 40 C° to 80 °C) and humidity up to 100% (**Figure S8**). From a practical point of view, NHs-based sensors are much more adapted for applications requiring precise strain measurements, such as in health monitoring devices or electronic skin, including harsh environments.

To further assess the mechanical stability of NHs-based sensors, a series of thousands and millions of loading cycles (each loading cycle going up to 0.036% tensile strain) were performed using a Key Life Test Machine (ZL-2806) followed by a measurement of the sensitivity using a three-point bending set-up. Results (**Figure 9**) show that NH@MPA$_{100}$ sensors retain their sensitivity even after 2 million consecutive cycles (with no rest) with very little loss of sensitivity.

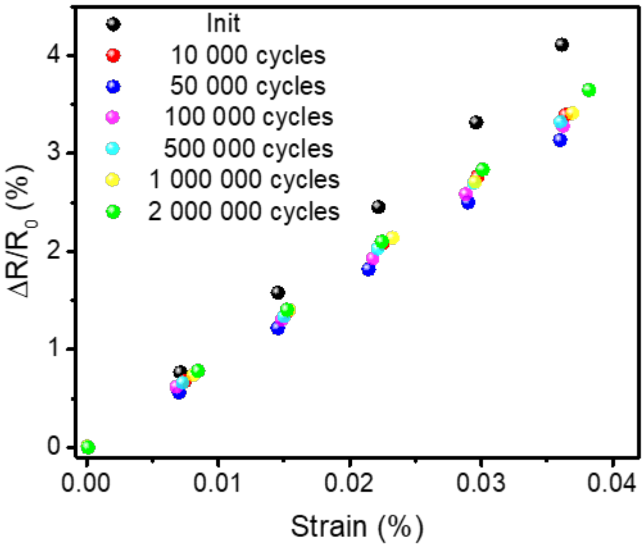

Figure 9. Relative variation of the resistance as a function of the applied strain after different series of loading cycles, where each loading cycle goes up to 0.036% tensile strain. « Init » refers to the measurement before subjecting to any cycling test.

We further tested these NHs-based sensors for electronic skin and healthcare applications. Before applying the sensor to a hand, the sensor is calibrated to obtain the relative variation of the resistance with the applied force. The relative changes in electrical resistance are measured using a three-point bending machine, as shown in **Figure S10a**. It is evaluated based on electrical resistance changes in small stepwise increments in force value. Eventually, a measured variation of the resistance of the sensor corresponding to the force generated by a finger is estimated using the graph generated with the same sensor showing the resistance variation with the applied force in Newton, **(Figure S10b**).

We then monitored the detection of hand motion by placing the sensor on the back of the hand, a particularly relevant location since the hand plays an important role as a primary part of the body by which humans sustain tactile interaction with their environment. The sensor is mounted on the center of the opisthenar on a typical glove with associated electrical connections. The problem associated with the direct attachment of the sensor in the hand module can include hand tremors and temperature. To reduce signal noise adhesive tape (green) is added right over the active sensing area to secure the sensor to the hand, as shown in **Figure S11a.** The experiment involves testing two different configurations of the sensor positioning, (**Figure S12a**). The sensor is placed on the back of the hand to be able to recognize small finger movements. The two different configurations are rotated 90° in relation to each other. The same applies to the NHs which, when deposited between the electrode gaps by DEP, are aligned almost parallel to each other. This means that, in configuration 1, these 1D nanomaterials are parallel to the motion of the hand while in configuration 2 they are positioned at 90° to the direction of their stretching. Both configurations reveal the high sensing accuracy of the NHs network. Indeed, the sensor can pick up the difference in positioning of the movement of the interdigital electrodes, from configuration 1 to configuration 2. Closing of the wrist causes the sensor to bend, therefore increasing the resistance value, while in Configuration 2, a sliding motion between the electrodes is recorded, as shown in **Figure S12b**, leading to a decrease in resistance.

We further tested these NHs-based sensors for pulse measurements, with the center of the sensing area (interdigitated electrodes) of the strain sensor placed on the radial artery, where there is a relatively strong beating pulse signal on a wrist. The overall is wrapped with a layer of adhesive tape. Because of the small size of the active sensing area and rigidness of the film, a constant and small pressure is held that helps to detect better the response (**Figure S13a**). the two ends of the sensor are connected to a Vector Network Analyzer (VNA) Instrument and a constant voltage of 0.5V is applied to the strain sensor, (**Figure S13b**). The test results illustrated in **Figure S14** show the real-time original signals measured with and without pulse wave; the signal with the pulse wave clearly shows periodic peaks (for comparison, in **Figure S14b**, only, noise is recorded. The three peaks of a pulse, systolic (Ps), inflection (Pi), and dicrotic peak (Pd) can be identified. The dicrotic peak (Pd) is known to be the result of the reflected pulse waves from the lower extremities and aorta. The difference in nominal current value in the two graphs is representative of slight pressure applied in the case of pulse detection measurement to better adapt to the curve of the hand and detect the response. Because of the small size of the active sensing area and rigidness of the chosen Kapton film (127μm thickness) the NHs-based sensor requires additional pressure to place it closer to the surface of the wrist. This pressure can be applied manually, using adhesive tape, or by simply wearing it under a watch.

Figure S14c displays the results of the measurement of an arterial pulse waveform and a close-up view of one cycle from a 25-year-old female subject. The arterial waveform can be significant in monitoring physiological conditions of the human cardiovascular system for possible future applications in medical diagnostic systems. High-resolution measurement is essential for reliable pulse diagnosis and here such a NHs-based sensor can reveal tiny feature variations in the pulse wave, in which the majority of currently used sensors in arterial tonometry are inefficient. This NHs-based sensor can more accurately and distinctly show the wrist pulse response, since the data presented are raw and without any treatment as in other cases.[62-63] The small size of the device (the active strain-sensing area is only 16mm^2) is also a key feature to improve wearability for continuous, real-time, and elaborate pulse monitoring at home. It needs minimal amplification and additional circuitry.

CONCLUSION

A new strain sensor was presented based on a piezoresistive nanomaterial made of gold nanoparticles covalently attached to the surface of silica nanohelices. Modifying the composition of the ligand mixture on the AuNP surface allows (i) tuning the colloidal stability of NH@AuNPs nanocomposite suspensions and (ii) controlling aggregation and degradation. These suspensions were perfectly adapted for the deposition of nano-objects between interdigitated electrodes using dielectrophoresis. DEP allowed precise and efficient deposition of NH@AuNPs in between the electrodes without any loss of material. This technique allowed precise control of the initial resistance of sensors. A sensitivity 60 times higher than that of a conventional metallic strain gauge was obtained. The obtained NHs-based sensors exhibit highly stable and reproducible electromechanical responses during long-term bending cycles. The use of NHs as templates for AuNPs improved the performance of the sensors in terms of sensitivity, hysteresis, and stability ($2x10^6$ cycles) thanks to preferential 1D electrical conduction pathway and 1D mechanical properties. Such improved electro-mechanical responses make them promising candidates for future wearable sensor technology, health monitoring, or electronic-skin applications. Indeed, health monitoring devices can measure various health metrics such as heart rate, blood pressure, body temperature, and other vitals and can be used to detect potential health problems. The use of flexible highly sensitive strain sensors is then, particularly relevant.[11, 16, 20]

MATERIAL AND METHODS

General. Tetraethoxysilane (TEOS) (> 99%), L/D tartaric acid (99.5%), $HAuCl_4$ (> 99.995%); trisodium citrate, mercaptopropionic acid (MPA), and N- hydroxy succinimide (NHS) (3-aminopropyl) triethoxysilane (APTES) (>99%) were purchased from Aldrich. O-(2-Carboxyethyl)-O'-(2-mercaptoethyl) heptaethylene glycol (SH-PEG7-COOH) (> 98%) was purchased from BioChemPeg and 1-ethyl-3-(3-dimethyl aminopropyl)-carbodiimide hydrochloride (EDC.HCl) (> 98%) from Alfa Aesar. The solvents were also purchased from Aldrich. Chemicals were used without further purification.

Synthesis of 16-2-16 Gemini Tartrate and Organic Nanohelices Formation. The 16-2-16 amphiphiles with tartrate counter-ions are synthesized according to previously published data.[42, 48, 64-65] To prepare the organic gel, Gemini tartrate powder (3.58 mg) is dissolved in 5 mL of MilliQ water (R = 18.2 MΩ) to obtain a 1 mM concentration of Gemini tartrate. The solution is sonicated for 5 min. It is then heated up to 70 °C (above the 16-2-16 tartrate Kraft temperature at 43 °C) for 10 min for complete dissolution. The solution is finally incubated at 20 °C for 3 days.

Preparation of Silica Nanohelices. Once the adequate aging time of the gels is reached, these organic self-assemblies are used as templates to prepare silica nanostructures through a sol-gel transcription procedure. In a typical preparation, tetraethoxysilane (TEOS, 500 μL) is added to the 10 mL of 0.1 mM aqueous solution of L-tartaric acid (pH 3.8) and prehydrolyzed at 20 °C by stirring on the roller-mixer for 7 h. In parallel, a solution of 1 mM 16-2-16 Gemini surfactant with L-tartrate counter ion is aged for 3 days for the formation of nanohelices, respectively. Equal volumes of prehydrolyzed TEOS in 0.1 mM aqueous solution of L-tartaric acid and organic gels are mixed (typically, 5 mL of each) and stirred at 20 °C on a roller-mixer overnight. Once the transcription is completed, the mixture is washed thoroughly with isopropanol, to solubilize the organic byproducts and eliminate the excess of TEOS (washing 5 times with absolute isopropanol by centrifugation (12 min, 4000 g) and redispersion in isopropanol). Typically, from 0.36 mg of organic gel, 5 mg of silica nanohelices were obtained.

Fragmentation of nanohelices.[48] After silica nanohelices are obtained, they are centrifuged and redispersed in ethanol and followed by tip sonication with various parameters to individualize and shorten the nanohelices and remove the aggregation of the nanohelices. A high-intensity ultrasonic processor (Vibra cell 75186) equipped with a 6 mm micro-tip with variable power was used (maximum power, 130 W). A 20 kHz pulse mode was chosen for the dispersion and fragmentation of silica nanohelices. The sonication time was varied from 1 min to 20 min and all the other experimental parameters are kept constant: sample concentration (1 mg/mL), volume (4 mL), power (130 W), and sonication time (20 min with pulses of 1 s separated by 1 s pauses). Samples are cooled in an ice bath during the sonication process to avoid solvent evaporation and rising of the sample temperature, which could influence the sonication.

Amine Functionalization of Silica Nanohelices. The silica nanohelices are then functionalized via a surface chemical modification with APTES. Generally, 10 µL of APTES are added per mg of short silica nanohelices in ethanol. The reaction mixture was submitted to ultrasonication for 5 min and, then kept in an oil bath overnight at 70 °C, followed by five times washing by centrifugation in absolute ethanol.

Synthesis of AuNPs. Tannic Acid/Citrate Stabilized AuNPs (TA-AuNPs). Gold nanoparticles with approximately 10 nm diameter are synthesized according to the procedure reported by Slot and Geuze[44] using both tannic acid and trisodium citrate as reducing and capping agents. To make 100 mL of an AuNPs suspension, two stock solutions are prepared: Solution A: 1 mL of 1% aqueous $HAuCl_4$ in 80 mL of Milli-Q water and Solution B: 4 mL of 1% trisodium citrate·$2H_2O$, and 0.1 mL of tannic acid in 16 mL of milli-Q water. Solutions A and B are heated to 60 °C, then solution B is added to solution A while stirring. After the solution turns red, it is heated further up to 100 °C for 1 h and then cooled down to room temperature.

AuNPs Surface Ligand Exchange. Tannic acid on the surface of AuNPs was exchanged with a molar % mixture of two ligands: O-(2-carboxyethyl)-O′-(2-mercapto ethyl) hexaethylene glycol (noted hereafter HS-PEG_7-COOH) and mercaptopropionic acid (MPA) to obtain PEG_{100}, MPA_{100}, or MPA_xPEG_{1-x} modified NPs. For instance, for the preparation of MPA_{100}, 8 mL of 8.56 nM 10 nm-TA-AuNPs are separated into 4 tubes of 2 mL, the tubes are centrifuged (21 000 g, 20 min) and 1.5 mL of supernatant was removed. Then, 0.5 mL of 1 mM MPA and 1 mM NaOH aqueous solution were added to each tube, followed by 5 min sonication, and then incubated at 4 °C overnight. After the reaction, AuNPs with MPA were precipitated by centrifugation and washed with water (centrifugation 21 000 g during 20 min, removal of the upper phase, combination of 2 tubes together, addition of water, vigorous shaking, and again). Finally, MPA_{100} was dispersed in 0.5 mL of water (134 nM) and kept at 20 °C before any use.

Synthesis of Gold grafted helices (NH@AuNPs) after Ligand Exchange. After ligand exchange, AuNPs were covalently grafted to the amino-functionalized nanohelices by activation of the CO_2H group using EDC/NHS activation.[49-51] Typically, 0.5 mL of an EDC/NHS aqueous solution (1.2 mM / 6.0 mM) was added to the 0.5mL MPA_{100} previously obtained. The dispersion was sonicated for 10 min and stirred at 4 °C for about 2 h. 50 µL of amino-functionalized nanohelices (~1 mg/mL) in ethanol were then added. Sonication was applied for 10 min to mix nanohelices and AuNPs homogeneously. The solution was then stirred overnight at room temperature on a rotary shaker. Finally, the suspension of AuNPs with silica nanohelices was washed 3 times by centrifugation and redispersion in water. For other MPA/PEG ratios see **Table 2**.

Deposition of NH@AuNPs. The strain sensors consisted of NH@AuNPs deposited between interdigitated electrodes. The thin gold electrodes (Au (200 nm) on Ti (50 nm)) were deposited by sputtering on a flexible 125 µm-thick polyimide substrate and structured using photolithography (Supplementary Information). The deposition of NH@AuNPs was done by DEP. A 20-µL droplet of NH@AuNPs (concentration 0.01mg/mL) was dropped to cover the electrodes entirely. An AC voltage (35 kHz - 10 V_{pp}) was applied between the electrodes during a controlled time (10 s to 10 min) to induce deposition. The drop was then quickly removed, and the electrode was dried at room temperature. Finally, the sensor active area was passivated using a thin-film encapsulating layer (Kapton Dupont) to improve its stability and avoid degradation due to dust or moisture. For comparison, a sensor based on free AuNPs was produced using the same electrodes with a deposition performed by drop-casting.

Methods

The study of localized surface plasmon resonance (LSPR) (aggregation of the AuNPs) was performed with a Cary 300 UV-vis spectrometer. Data were recorded with a 1.0 nm data interval and a 600 nm/min scan rate in 10 mm-optical path length quartz cuvettes. Samples were analyzed using a Nicolet Nexus 870 FT-IR spectrometer with a Mercury Cadmium Telluride (MCT) detector with a 4 cm^{-1} spectral resolution. Samples were deposited on a germanium crystal and dried with nitrogen flow. A mean spectrum was obtained from 200 spectra. ATR measurements were done on a Nicolet Summit apparatus, with an IR source and a DTGS KBr detector. The data was collected by superimposing 32 scans carried out over the 400 cm^{-1} to 4000 cm^{-1} range for 46.9 seconds.

SEM images were obtained with a Hitachi S-4800 high-resolution SEM. TEM was performed at room temperature on a Philips EM 120 electron microscope operating at 120 kV, and the images were collected with a 2k × 2k Gatan CCD camera. Drops of diluted dispersions of the nanocomposite were deposited on carbon film-coated 200/400-mesh copper grids. The excess liquid was blotted with filter paper. Visualization and quantitative analysis of the final volumes were carried out by using ImageJ software.

Piezoresistive characterization. The initial resistance of the sensor, *i.e.*, the resistance at rest, R_0, and the sensor piezoresistive response, *i.e.*, the relative resistance variation under strain, were measured using two similar three-point bending benches (namely, a Mark-10 ESM303 with an M5-2 dynamometer, and a Mark-10 ESM301L with an M5-5 dynamometer). The source meter units associated with both benches (Keithley DMM6500 and Keithley 2450, respectively) provided a constant current of 10 μA. To do so, the sensors were glued on the center of a PET plate (500 μm thick) or 1mm-thick glass slide and bent the deformed plate using a three-point bending test (Mark 10 ESM303 with a force sensor M5-2). The resistance was measured while applying a deformation using a source meter (Keithley DMM6500) at a constant current (10 μA).

Both tensile strain ($\varepsilon > 0$) and compressive strain ($\varepsilon < 0$) were applied with the same setup, whether the sensor was below or above the substrate. The strain (ε) imposed on the sensors was determined from the vertical displacement (Δz) imposed on the substrate or from the force applied on the substrate (F). From the classical beam theory, strain is given by $\varepsilon = (6(e_1 + 2e_2)\Delta z)/{L_0}^2$, where $e_1$is the thickness of the substrate, e_2 is the thickness of the sensor and L_0 is the distance between the two underlying points of the three-point bending bench.[66] A higher precision on the strain is achieved when the force (F) is used instead of the vertical displacement. Preliminarily, calibration measurements connecting the applied force with the associated applied strain were performed in working conditions. These measurements consisted in recording the resistance variations of well-known commercial strain gauges (RadioSpare #865-6235 GF = 2) in said conditions.

Cyclability test conditions. Load cycle tests were performed using an automatic load cycle machine, Key Life Test Machine (ZL – 2806). The strain sensors were glued on a glass slide and positioned on a three-point test bench. The frequency of load cycles was set to 1 Hz. After performing up to 2 million cycles (about 23 days), the sensors were still fully functional, with no significant sensitivity degradation.

ASSOCIATED CONTENT

Supporting Information. Additional data and figures are included in the Supplementary Information. **Figure S1.** UV vis spectra of AuNPs with various ratios of MPA and PEG ligands. To avoid aggregation of the AuNPs@MPA_{100} the pH of the solution was stabilized at 5.6 *i.e.* above the pKa of MPA. **Figure S2**. TEM images of the a) AuNPs@$MPA_{100}PEG_0$, b) AuNPs@$MPA_{50}PEG_{50}$ c) AuNPs@MPA_0PEG_{100} illustrate the increased distance between particles. **Figure S3**. TEM images showing a) the starting silica Nanohelices and the results of the covalent grafting of the AuNPs@$MPA_{100}PEG_0$, AuNPs@$MPA_{75}PEG_{25}$, AuNPs@$MPA_{50}PEG_{50}$, and AuNPs@MPA_0PEG_{100} on the silica Nannohelices using two ratios of EDC/NHS reactants1.2/6.0 mM((b)-(e)), and 12/60 mM ((f)-(i)). **Figure S4**. a) ATR infrared spectrum of NHs@MPA_{100} in between 1,000 cm^{-1} and 3,000 cm^{-1}. b) ATR infrared spectra of MTA, AuNPsMPA$_{100}$, NHs@MPA_{100} showing the modification of the peak position with the different processes. **Figure S5.** a) aNormalized UV-Vis absorption spectra of NHs@AuNPs obtained for different AuNPs surface compositions: AuNPs@$MPA_{100}PEG_0$, AuNPs@$MPA_{75}PEG_{25}$, AuNPs@$MPA_{50}PEG_{50}$, and AuNPs@MPA_0PEG_{100}; b) CD spectra of the same NHs@AuNPs normalized with respect to the absorbance spectra. **Figure S6**. A step-by-step fabrication process for interdigitated electrodes on polyimide: a) top view, b) cross-sectional view. In the cross-sectional view: (I) a 4inch p-type silicon wafer used as a hard substrate, (II) PDMS layer spin-coated on the silicon wafer, (III) a polyimide (PI) lamination, (IV) deposition of a negative photoresist (PR) layer (nLOF) and transfer of the mask pattern onto the PR layer, (V) development for 30 seconds (VI) sputtering of a bilayer of Ti/Au (50 nm/200 nm), (VII) lift-off and (VIII) delamination and cutting of the PI layer; c) Detailed scheme of the electrodes at various scales; d) interdigitated electrodes over silicon dioxide substrate, glass substrate, and polyimide substrate. **Figure S7**. Dielectrophoresis *vs*. Drop-Cast; (a-c) Results of DEP deposition; (d-f) Results of Drop-Cast at various magnifications in the case of AuNPs deposition. **Figure S8**. Temperature and humidity tests for our strain sensors a) Resistance variations of encapsulated and non-encapsulated NHs-based sensors at low temperature (-40°C) b) Resistance variation of encapsulated and non-encapsulated NHs-based sensors at high temperature (80°C), c) Humidity cycle-resistance variations of encapsulated and non-encapsulated NHs-based sensors during a humidity cycle. **Figure S9.** Relative variation of the resistance as a function of the applied strain after 10 000 and 2 000 000 cycles series of loading cycles, where each loading cycle goes up to 0.036% tensile strain. « Init » refers to the measurement before subjecting to any cycling test. Extract from Figure 9 to exhibit the 10 000-cycle response. **Figure S10.** a) Three-point bending set-up b) Representative calibration curve. The sensor is calibrated before being installed on the subject. Force output in Newton is synchronized with resistance variation to produce a calibration equation, which is used subsequently to convert the resistance variation data from all trials on finger/hand into units of force. The fit for this sensor is linear with an R^2 value of 0.9. **Figure S11.** a) Photograph and b) the layout of the sensors on the gloved hand; c) bending (1s) and relaxation (5s) tests were performed. **Figure S12**. a) Demonstration of real-time tracking of the hand bending by the NHs stretch sensor glove for two different configurations; b) Resistance response of configuration 1 and configuration 2. The particular case, Configuration 2, shown here tracks the ultralow sliding effect between the electrodes. **Figure S13**. a) Photograph images of an

NHs-based strain sensor attached to the wrist using adhesive tape to monitor pulse (hand on top of the image); b) Electronic circuit diagram for measuring the resistance change of the sensor due to geometrical deformation of the microchannel. **Figure S14.** Real-time pulse wave and small strain sensing performance, original signals measured a) with and b) without pulse detection; c) A close-up view of one cycle showing three peaks: ① systolic (Ps), ② inflection (Pi), ③ dicrotic (Pd) peaks.

"This material is available free of charge via the Internet at http://pubs.acs.org."

AUTHOR INFORMATION

Corresponding Authors

Delville M-H - *CNRS, Univ. Bordeaux, Bordeaux INP, ICMCB, UMR 5026, 87 avenue du Dr. A. Schweitzer, Pessac, F-33608, France.* http://orcid.org/0000-0001-8863-8225 Email: marie-helene.delville@icmcb.cnrs.fr

Oda R. - *CNRS, Univ. Bordeaux, Bordeaux INP, Chimie et Biologie des Membranes et des Nanoobjets, 33607 Pessac, France.* https://orcid.org/0000-0003-3273-8635 Email: reiko.oda@u-bordeaux.fr

Bergaud C. - *CNRS, Laboratoire d'Analyse et d'Architecture des Systèmes, LAAS-CNRS, University of Toulouse, 7 avenue du Colonel Roche, Toulouse, F-31400, France.* https://orcid.org/0000-0003-0093-9600 Email: Christian Bergaud bergaud@laas.fr

ACKNOWLEDGMENT

The authors want to gratefully acknowledge the financial support of the “Agence Nationale de la Recherche” grant n° ANR-15-CE08-0041 (NANOHELIFLEX). This work was partly supported by the French Renatech network.

REFERENCES

1. Kang, M.; Kim, J.; Jang, B.; Chae, Y.; Kim, J.-H.; Ahn, J.-H., Graphene-Based Three-Dimensional Capacitive Touch Sensor for Wearable Electronics. *ACS Nano* **2017,** *11*, 7950-7957,

2. Singh, P.; Baek, S.; Yoo, H. H.; Niu, J.; Park, J.-H.; Lee, S., Two-Dimensional CIPS-InSe van der Waal Heterostructure Ferroelectric Field Effect Transistor for Nonvolatile Memory Applications. *ACS Nano* **2022,** *16*, 5418-5426,

3. Wan, Y.; Wang, Y.; Guo, C. F., Recent Progress on Flexible Tactile Sensors. *Materials Today Physics* **2017,** *1*, 61-73,

4. Tang, X.; Yang, W.; Yin, S.; Tai, G.; Su, M.; Yang, J.; Shi, H.; Wei, D.; Yang, J., Controllable Graphene Wrinkle for a High-Performance Flexible Pressure Sensor. *ACS Applied Materials & Interfaces* **2021,** *13*, 20448-20458,

5. Liang, C.; Sun, J.; Liu, Z.; Tian, G.; Liu, Y.; Zhao, Q.; Yang, D.; Chen, J.; Zhong, B.; Zhu, M.; Xu, H.; Qi, D., Wide Range Strain Distributions on the Electrode for Highly Sensitive Flexible Tactile Sensor with Low Hysteresis. *ACS Applied Materials & Interfaces* **2023,** *15*, 15096-15107,

6. Amjadi, M.; Kyung, K.-U.; Park, I.; Sitti, M., Stretchable, Skin-Mountable, and Wearable Strain Sensors and Their Potential Applications: A Review. *Advanced Functional Materials* **2016,** *26*, 1678-1698,

7. Seyedin, S.; Zhang, P.; Naebe, M.; Qin, S.; Chen, J.; Wang, X.; Razal, J. M., Textile Strain Sensors: a Review of the Fabrication Technologies, Performance Evaluation, and Applications. *Materials Horizons* **2019,** *6*, 219-249,

8. Lu, Y.; Liu, Z.; Yan, H.; Peng, Q.; Wang, R.; Barkey, M. E.; Jeon, J.-W.; Wujcik, E. K., Ultrastretchable Conductive Polymer Complex as a Strain Sensor with a Repeatable Autonomous Self-Healing Ability. *ACS Applied Materials & Interfaces* **2019,** *11*, 20453-20464,

9. Dong, W.; Li, W.; Tao, Z.; Wang, K., Piezoresistive Properties of Cement-Based Sensors: Review and Perspective. *Construction and Building Materials* **2019,** *203*, 146-163,

10. Segev-Bar, M.; Haick, H., Flexible Sensors Based on Nanoparticles. *ACS Nano* **2013,** *7*, 8366-8378,

11. Huang, C.-B.; Yao, Y.; Montes-García, V.; Stoeckel, M.-A.; Von Holst, M.; Ciesielski, A.; Samorì, P., Highly Sensitive Strain Sensors Based on Molecules-Gold Nanoparticles Networks for High-Resolution Human Pulse Analysis. *Small* **2021,** *17*, 2007593,

12. Cheng, H.-W.; Yan, S.; Shang, G.; Wang, S.; Zhong, C.-J., Strain Sensors Fabricated by Surface Assembly of Nanoparticles. *Biosensors and Bioelectronics* **2021,** *186*, 113268,

13. Yi, J.; Xianyu, Y., Gold Nanomaterials-Implemented Wearable Sensors for Healthcare Applications. *Advanced Functional Materials* **2022,** *32*, 2113012,

14. Liu, H.; Li, Q.; Zhang, S.; Yin, R.; Liu, X.; He, Y.; Dai, K.; Shan, C.; Guo, J.; Liu, C.; Shen, C.; Wang, X.; Wang, N.; Wang, Z.; Wei, R.; Guo, Z., Electrically Conductive Polymer Composites for Smart Flexible Strain Sensors: a Critical Review. *Journal of Materials Chemistry C* **2018,** *6*, 12121-12141,

15. Duan, L.; D'Hooge, D. R.; Cardon, L., Recent Progress on Flexible and Stretchable Piezoresistive Strain Sensors: From Design to Application. *Progress in Materials Science* **2020,** *114*, 100617,

16. Jheng, W.-W.; Su, Y.-S.; Hsieh, Y.-L.; Lin, Y.-J.; Tzeng, S.-D.; Chang, C.-W.; Song, J.-M.; Kuo, W., Gold Nanoparticle Thin Film-Based Strain Sensors for Monitoring Human Pulse. *ACS Applied Nano Materials* **2021,** *4*, 1712-1718,

17. Chen, M.; Luo, W.; Xu, Z.; Zhang, X.; Xie, B.; Wang, G.; Han, M., An Ultrahigh Resolution Pressure Sensor Based on Percolative Metal Nanoparticle Arrays. *Nature Communications* **2019,** *10*, 4024,

18. Lee, W. S.; Jeon, S.; Oh, S. J., Wearable Sensors Based on Colloidal Nanocrystals. *Nano Convergence* **2019,** *6*, 10,

19. Choi, S.; Han, S. I.; Kim, D.; Hyeon, T.; Kim, D.-H., High-Performance Stretchable Conductive Nanocomposites: Materials, Processes, and Device Applications. *Chemical Society Reviews* **2019,** *48*, 1566-1595,

20. Zang, Y.; Zhang, F.; Di, C.-a.; Zhu, D., Advances of Flexible Pressure Sensors Toward Artificial Intelligence and Health Care Applications. *Materials Horizons* **2015,** *2*, 140-156,

21. Ly, T. N.; Park, S., Wearable Strain Sensor for Human Motion Detection Based on Ligand-Exchanged Gold Nanoparticles. *Journal of Industrial and Engineering Chemistry* **2020,** *82*, 122-129,

22. Olichwer, N.; Leib, E. W.; Halfar, A. H.; Petrov, A.; Vossmeyer, T., Cross-Linked Gold Nanoparticles on Polyethylene: Resistive Responses to Tensile Strain and Vapors. *ACS Applied Materials & Interfaces* **2012,** *4*, 6151-6161,

23. Ketelsen, B.; Yesilmen, M.; Schlicke, H.; Noei, H.; Su, C.-H.; Liao, Y.-C.; Vossmeyer, T., Fabrication of Strain Gauges via Contact Printing: A Simple Route to Healthcare Sensors Based on Cross-Linked Gold Nanoparticles. *ACS Applied Materials & Interfaces* **2018,** *10*, 37374-37385,

24. Moreira, H.; Grisolia, J.; Sangeetha, N. M.; Decorde, N.; Farcau, C.; Viallet, B.; Chen, K.; Viau, G.; Ressier, L., Electron Transport in Gold Colloidal Nanoparticle-Based Strain Gauges. *Nanotechnology* **2013,** *24*, 095701,

25. Daruich De Souza, C.; Ribeiro Nogueira, B.; Rostelato, M. E. C. M., Review of the Methodologies Used in the Synthesis Gold Nanoparticles by Chemical Reduction. *Journal of Alloys and Compounds* **2019,** *798*, 714-740,

26. Herrmann, J.; Müller, K.-H.; Reda, T.; Baxter, G. R.; Raguse, B.; Groot, G. J. J. B. d.; Chai, R.; Roberts, M.; Wieczorek, L., Nanoparticle Films as Sensitive Strain Gauges. *Applied Physics Letters* **2007,** *91*, 183105,

27. Amjadi, M.; Pichitpajongkit, A.; Lee, S.; Ryu, S.; Park, I., Highly Stretchable and Sensitive Strain Sensor Based on Silver Nanowire-Elastomer Nanocomposite. *ACS Nano* **2014,** *8*, 5154-5163,

28. Tanner, J. L.; Mousadakos, D.; Giannakopoulos, K.; Skotadis, E.; Tsoukalas, D., High Strain Sensitivity Controlled by the Surface Density of Platinum Nanoparticles. *Nanotechnology* **2012,** *23*, 285501,

29. Li, C.; Thostenson, E. T.; Chou, T.-W., Dominant Role of Tunneling Resistance in the Electrical Conductivity of Carbon Nanotube-Based Composites. *Applied Physics Letters* **2007,** *91*, 223114,

30. Gao, J.; Huang, X.; Liu, H.; Zan, F.; Ren, J., Colloidal Stability of Gold Nanoparticles Modified with Thiol Compounds: Bioconjugation and Application in Cancer Cell Imaging. *Langmuir* **2012,** *28*, 4464-4471,

31. Lee, S. W.; Joh, H.; Seong, M.; Lee, W. S.; Choi, J. H.; Oh, S. J., Engineering Surface Ligands of Nanocrystals to Design High Performance Strain Sensor Arrays through Solution Processes. *Journal of Materials Chemistry C* **2017,** *5*, 2442-2450,

32. Cheng, J.; Le Saux, G.; Gao, J.; Buffeteau, T.; Battie, Y.; Barois, P.; Ponsinet, V.; Delville, M.-H.; Ersen, O.; Pouget, E.; Oda, R., GoldHelix: Gold Nanoparticles Forming 3D Helical Superstructures with Controlled Morphology and Strong Chiroptical Property. *ACS Nano* **2017,** *11*, 3806-3818,

33. Gao, J.; Wu, W.; Lemaire, V.; Carvalho, A.; Nlate, S.; Buffeteau, T.; Oda, R.; Battie, Y.; Pauly, M.; Pouget, E., Tuning the Chiroptical Properties of Elongated Nano-objects via Hierarchical Organization. *ACS Nano* **2020,** *14*, 4111-4121,

34. Sangeetha, N. M.; Decorde, N.; Viallet, B.; Viau, G.; Ressier, L., Nanoparticle-Based Strain Gauges Fabricated by Convective Self Assembly: Strain Sensitivity and Hysteresis with Respect to Nanoparticle Sizes. *The Journal of Physical Chemistry C* **2013,** *117*, 1935-1940,

35. Segev-Bar, M.; Landman, A.; Nir-Shapira, M.; Shuster, G.; Haick, H., Tunable Touch Sensor and Combined Sensing Platform: Toward Nanoparticle-based Electronic Skin. *ACS Applied Materials & Interfaces* **2013,** *5*, 5531-5541,

36. Hwang, H.; Kim, Y.; Park, J.-H.; Jeong, U., 2D Percolation Design with Conductive Microparticles for Low-Strain Detection in a Stretchable Sensor. *Advanced Functional Materials* **2020,** *30*, 1908514,

37. Rycewicz, M.; Ficek, M.; Gajewski, K.; Kunuku, S.; Karczewski, J.; Gotszalk, T.; Wlasny, I.; Wysmołek, A.; Bogdanowicz, R., Low-Strain Sensor Based on the Flexible Boron-Doped Diamond-Polymer Structures. *Carbon* **2021,** *173*, 832-841,

38. Zheng, M.; Li, W.; Xu, M.; Xu, N.; Chen, P.; Han, M.; Xie, B., Strain Sensors Based on Chromium Nanoparticle Arrays. *Nanoscale* **2014,** *6*, 3930-3933,

39. Liao, X.; Zhang, Z.; Liang, Q.; Liao, Q.; Zhang, Y., Flexible, Cuttable, and Self-Waterproof Bending Strain Sensors Using Microcracked Gold Nanofilms@Paper Substrate. *ACS Applied Materials & Interfaces* **2017,** *9*, 4151-4158,

40. Radha, B.; Sagade, A. A.; Kulkarni, G. U., Flexible and Semitransparent Strain Sensors Based on Micromolded Pd Nanoparticle–Carbon μ-Stripes. *ACS Applied Materials & Interfaces* **2011,** *3*, 2173-2178,

41. Wang, X.; Liu, X.; Ge, X.; Schubert, D. W., Superior sensitive, high-tensile flexible fabric film strain sensor. *Composites Part A: Applied Science and Manufacturing* **2023,** *172*, 107610,

42. Delclos, T.; Aimé, C.; Pouget, E.; Brizard, A.; Huc, I.; Delville, M.-H.; Oda, R., Individualized Silica Nanohelices and Nanotubes: Tuning Inorganic Nanostructures Using Lipidic Self-Assemblies. *Nano Letters* **2008,** *8*, 1929-1935,

43. Tamoto, R.; Lecomte, S.; Si, S.; Moldovan, S.; Ersen, O.; Delville, M.-H.; Oda, R., Gold Nanoparticle Deposition on Silica Nanohelices: A New Controllable 3D Substrate in Aqueous Suspension for Optical Sensing. *The Journal of Physical Chemistry C* **2012,** *116*, 23143-23152,

44. Slot, J. W.; Geuze, H. J., A New Method of Preparing Gold Probes for Multiple-Labeling Cytochemistry. *Eur J Cell Biol* **1985,** *38*, 87-93,

45. Rahme, K.; Chen, L.; Hobbs, R. G.; Morris, M. A.; O'Driscoll, C.; Holmes, J. D., PEGylated Gold Nanoparticles: Polymer Quantification as a Function of PEG Lengths and Nanoparticle Dimensions. *RSC Advances* **2013,** *3*, 6085-6094,

46. Hinterwirth, H.; Kappel, S.; Waitz, T.; Prohaska, T.; Lindner, W.; Lämmerhofer, M., Quantifying Thiol Ligand Density of Self-Assembled Monolayers on Gold Nanoparticles by Inductively Coupled Plasma-Mass Spectrometry. *ACS Nano* **2013,** *7*, 1129-1136,

47. Gillich, T.; Acikgöz, C.; Isa, L.; Schlüter, A. D.; Spencer, N. D.; Textor, M., PEG-Stabilized Core-Shell Nanoparticles: Impact of Linear versus Dendritic Polymer Shell Architecture on Colloidal Properties and the Reversibility of Temperature-Induced Aggregation. *ACS Nano* **2013,** *7*, 316-329,

48. Okazaki, Y.; Cheng, J.; Dedovets, D.; Kemper, G.; Delville, M.-H.; Durrieu, M.-C.; Ihara, H.; Takafuji, M.; Pouget, E.; Oda, R., Chiral Colloids: Homogeneous Suspension of Individualized SiO_2 Helical and Twisted Nanoribbons. *ACS Nano* **2014,** *8*, 6863-6872,

49. Wang, C.; Yan, Q.; Liu, H.-B.; Zhou, X.-H.; Xiao, S.-J., Different EDC/NHS Activation Mechanisms between PAA and PMAA Brushes and the Following Amidation Reactions. *Langmuir* **2011,** *27*, 12058-12068,

50. Sam, S.; Touahir, L.; Salvador Andresa, J.; Allongue, P.; Chazalviel, J. N.; Gouget-Laemmel, A. C.; Henry de Villeneuve, C.; Moraillon, A.; Ozanam, F.; Gabouze, N.; Djebbar, S., Semiquantitative Study of the EDC/NHS Activation of Acid Terminal Groups at Modified Porous Silicon Surfaces. *Langmuir* **2010,** *26*, 809-814,

51. Park, C.; Vo, C. L.-N.; Kang, T.; Oh, E.; Lee, B.-J., New method and characterization of self-assembled gelatin–oleic nanoparticles using a desolvation method via carbodiimide/N-hydroxysuccinimide (EDC/NHS) reaction. *European Journal of Pharmaceutics and Biopharmaceutics* **2015,** *89*, 365-373,

52. Wang, H., Plasmonic Refractive Index Sensing Using Strongly Coupled Metal Nanoantennas: Nonlocal Limitations. *Scientific Reports* **2018,** *8*, 9589,

53. Sönnichsen, C.; Reinhard, B. M.; Liphardt, J.; Alivisatos, A. P., A Molecular Ruler Based on Plasmon Coupling of Single Gold and Silver Nanoparticles. *Nature Biotechnology* **2005,** *23*, 741-745,

54. Freer, E. M.; Grachev, O.; Duan, X.; Martin, S.; Stumbo, D. P., High-Yield Self-Limiting Single-Nanowire Assembly with Dielectrophoresis. *Nature Nanotechnology* **2010,** *5*, 525-530,

55. Vijayaraghavan, A.; Blatt, S.; Weissenberger, D.; Oron-Carl, M.; Hennrich, F.; Gerthsen, D.; Hahn, H.; Krupke, R., Ultra-Large-Scale Directed Assembly of Single-Walled Carbon Nanotube Devices. *Nano Letters* **2007,** *7*, 1556-1560,

56. Seichepine, F.; Salomon, S.; Collet, M.; Guillon, S.; Nicu, L.; Larrieu, G.; Flahaut, E.; Vieu, C., A Combination of Capillary and Dielectrophoresis-Driven Assembly Methods for Wafer Scale Integration of Carbon-Nanotube-Based Nanocarpets. *Nanotechnology* **2012,** *23*, 095303,

57. Shekhar, S.; Stokes, P.; Khondaker, S. I., Ultrahigh Density Alignment of Carbon Nanotube Arrays by Dielectrophoresis. *ACS Nano* **2011,** *5*, 1739-1746,

58. Lee, D. H.; Park, J.; Lee, J.-K.; Heo, K.; Lee, D.-J.; Lee, Y. R.; Lee, B. Y., Highly Sensitive and Flexible Strain Sensors Based on Patterned ITO Nanoparticle Channels. *Nanotechnology* **2017,** *28*, 495501,

59. Min, S.-H.; Lee, G.-Y.; Ahn, S.-H., Direct Printing of Highly Sensitive, Stretchable, and Durable Strain Sensor Based on Silver Nanoparticles/Multi-Walled Carbon Nanotubes Composites. *Composites Part B: Engineering* **2019,** *161*, 395-401,

60. Wang, B.; Facchetti, A., Mechanically Flexible Conductors for Stretchable and Wearable E-Skin and E-Textile Devices. *Advanced Materials* **2019,** *31*, 1901408,

61. Müller, K. H.; Wei, G.; Raguse, B.; Myers, J., Three-Dimensional Percolation Effect on Electrical Conductivity in Films of Metal Nanoparticles Linked by Organic Molecules. *Physical Review B* **2003,** *68*, 155407,

62. Meng, Q.; Liu, Z.; Han, S.; Xu, L.; Araby, S.; Cai, R.; Zhao, Y.; Lu, S.; Liu, T., A facile approach to fabricate highly sensitive, flexible strain sensor based on elastomeric/graphene platelet composite film. *Journal of Materials Science* **2019,** *54*, 10856-10870,

63. Shi, G.; Liu, T.; Kopecki, Z.; Cowin, A.; Lee, I.; Pai, J.-H.; Lowe, S. E.; Zhong, Y. L., A Multifunctional Wearable Device with a Graphene/Silver Nanowire Nanocomposite for Highly Sensitive Strain Sensing and Drug Delivery. *C* **2019,** *5*, 17,

64. Oda, R.; Huc, I.; Schmutz, M.; Candau, S. J.; MacKintosh, F. C., Tuning Bilayer Twist Using Chiral Counterions. *Nature* **1999,** *399*, 566-569,

65. Okazaki, Y.; Buffeteau, T.; Siurdyban, E.; Talaga, D.; Ryu, N.; Yagi, R.; Pouget, E.; Takafuji, M.; Ihara, H.; Oda, R., Direct Observation of Siloxane Chirality on Twisted and Helical Nanometric Amorphous Silica. *Nano Letters* **2016,** *16*, 6411-6415,

66. Madsen, N. D.; Kjelstrup-Hansen, J., Three-point Bending Setup for Piezoresistive Gauge Factor Measurement of Thin-Film Samples at High Temperatures. *Review of Scientific Instruments* **2017,** *88*, 015001,

TOC: